Integrative and Comparative Biology

Integrative and Comparative Biology, volume 63, number 6, pp. 1266–1276
https://doi.org/10.1093/icb/icad086

Society for Integrative and Comparative Biology

INVITED PAPER

Hydrodynamic Diversity of Jets Mediated by Giant and Non-Giant Axon Systems in Brief Squid

Diana H. Li [*,1,#], Ian K. Bartol [†] and William F. Gilly [*]

[*]Hopkins Marine Station, Stanford University, Pacific Grove, CA 93950, USA; [†]Department of Biological Sciences, Old Dominion University, Norfolk, VA 23539, USA

[#]Present address: Mortimer B. Zuckerman Mind Brain Behavior Institute, Columbia University, New York, NY.

[1]E-mail: dhl2137@columbia.edu

Synopsis Neural input is critical for establishing behavioral output, but understanding how neuromuscular signals give rise to behaviors remains a challenge. In squid, locomotion through jet propulsion underlies many key behaviors, and the jet is mediated by two parallel neural pathways, the giant and non-giant axon systems. Much work has been done on the impact of these two systems on jet kinematics, such as mantle muscle contraction and pressure-derived jet speed at the funnel aperture. However, little is known about any influence these neural pathways may have on the hydrodynamics of the jet after it leaves the squid and transfers momentum to the surrounding fluid for the animal to swim. To gain a more comprehensive view of squid jet propulsion, we made simultaneous measurements of neural activity, pressure inside the mantle cavity, and wake structure. By computing impulse and time-averaged forces from the wake structures of jets associated with giant or non-giant axon activity, we show that the influence of neural pathways on jet kinematics could extend to hydrodynamic impulse and force production. Specifically, the giant axon system produced jets with, on average, greater impulse magnitude than those of the non-giant system. However, non-giant impulse could exceed that of the giant system, evident by the graded range of its output in contrast to the stereotyped nature of the giant system. Our results suggest that the non-giant system offers flexibility in hydrodynamic output, while recruitment of giant axon activity can provide a reliable boost when necessary.

Introduction

Key components of animal locomotion are the motor patterns that give rise to coordinated muscular output and behavior. In squids, two parallel motor pathways, the giant and non-giant axon systems, underlie jet propulsion by mediating contractions of the squid's muscular mantle (Fig. 1; Young 1938). These two pathways are responsible for magnitudes and rates of mantle contraction, thus offering the basis for a variety of locomotor behaviors (Otis and Gilly 1990). Because the speed of the jet exiting the funnel is proportional to the square of the pressure inside the mantle, the magnitude of a mantle contraction can affect exit jet velocity and ultimately the squid's swimming speed (O'Dor 1988). A single action potential traveling along the giant axon system has long been known to elicit a strong, all-or-none muscle twitch of circular muscle fibers in the squid's mantle to produce a powerful jet (Young 1938; Packard 1969). In contrast, numerous non-giant axons are typically involved in weaker, graded mantle contractions, but repetitive signals from the non-giant system can summate to produce mantle twitches and resultant jets comparable to or exceeding those of the giant system acting alone (Otis and Gilly 1990; Gilly et al. 1996). Furthermore, the two neural pathways can act in concert to give rise to a range of jet magnitudes and latencies (Otis and Gilly 1990), thus bringing great interest to understanding the coordination of these two pathways in swimming.

Once a jet leaves the mantle, its interactions with the surrounding seawater can influence impulse and force production, as well as propulsive efficiency. Such hydrodynamic characteristics of squid jets have been studied in multiple species and at different life stages (Anderson and DeMont 2000; Bartol et al. 2001, 2008, 2009a, 2009b, 2016; Anderson and Grosenbaugh 2005).

Advance Access publication June 28, 2023

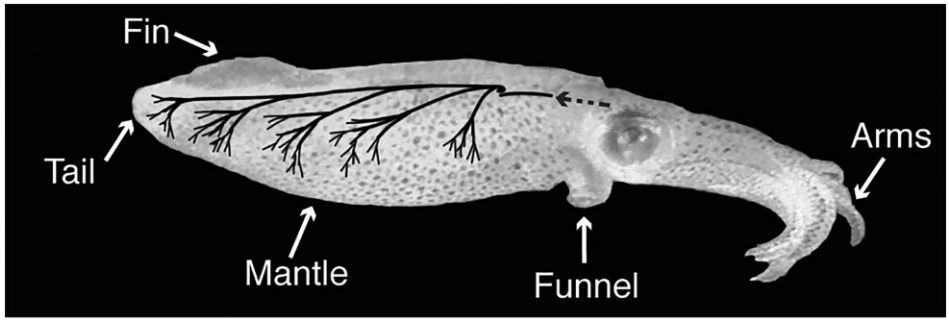

Fig. 1 Squid anatomy is involved in locomotion. Neural impulses from the brain (dashed arrow) control the mantle muscle through innervation by the stellar nerves (solid black lines), which are comprised of parallel pathways of giant and non-giant axons. By contracting the mantle muscle, squid produce pulsed jets directed through a maneuverable funnel, thus allowing them to swim in a variety of directions, including tail-first and arms-first swimming.

By contracting the mantle muscle, squid can produce an impulsive jet in the form of a vortex ring, a central hydrodynamic feature of biological propulsion. Vortex rings of jets generated mechanically using a piston inside a cylinder can play a critical role for momentum transfer and possible thrust augmentation by accelerating ambient fluid through added and entrained mass (Krueger and Gharib 2003, 2005).

Vortex ring structures give rise to two principal hydrodynamic modes based on general patterns of jet wake structures (Bartol et al. 2008, 2009b). Jets of mode 1 feature an isolated vortex ring with higher propulsive efficiency than longer jets, and such jets are often associated with slow swimming. Those of mode 2 involve a leading vortex ring that has pinched off from a long trailing jet and produce greater force than mode 1 jets, usually at faster swimming speeds (Bartol et al. 2008, 2009b). However, intermediate structures and more complex wakes falling outside of these categories have been revealed using 3D visualizing techniques able to capture features that are not fully resolved in the laser plane of traditional 2D methods (Bartol et al. 2016).

Despite the significant amount of research effort to understand the many aspects of squid locomotion, gaining a comprehensive view from neural mechanisms to muscular and hydrodynamic output has remained a challenge. To alleviate some logistical hurdles, studies on other animals have typically combined insights from experiments conducted separately on neuromuscular mechanisms and swimming hydrodynamics. For example, separate electromyography and wake visualization experiments suggest that trout reduce muscle recruitment to adopt energy-saving gaits depending on the flow surrounding them (Liao et al. 2003). In moon jellyfish, separate neuromuscular stimulation and wake visualization experiments validate fluid dynamic models showing elastic wave resonance in a flexible-bodied jet-propelled swimmer (Hoover et al. 2021). Avoiding the challenges of live animals, numerical simulations of resultant wake structures formed from activating different neuromuscular pathways in jellyfish have revealed the roles of pacemaker neurons and tissue elasticity in jet propulsion (Hoover et al. 2017). However, direct simultaneous measurements of motor neuron activity, muscular response, and behavioral output can offer insights into the diversity of locomotor behaviors that might remain undetected through independent measurements. Such studies relating neural activity to hydrodynamic output of jetting squid have not yet been reported.

Here, we combine *in viv o* recordings of neural activity and pressure inside the mantle cavity with defocusing digital particle tracking velocimetry (DDPTV) to visualize 3D wake structure of jets from brief squid (*Loliguncula brevis*) and provide the first concurrent observations across neural, kinematic, and hydrodynamic aspects of the squid jet. In aiming to reveal how the giant and non-giant axon systems influence jet hydrodynamics, we find that the roles played by each neural pathway in shaping kinematic elements like jet exit speed at the funnel aperture and mantle muscle mechanics also apply to the jet's impulse and force production.

Methods

We documented simultaneous pressure inside the mantle cavity, *en passant* extracellular stellar-nerve activity, and wake structure of jets produced by tethered *L. brevis* (5.9–7.0 cm dorsal mantle length [DML], $N = 3$).

Animals

Adult *L. brevis* were collected by otter trawl near the Virginia Institute of Marine Science's Eastern Shore Lab in Wachapreague, VA, USA, in October 2017. During transport to the Aquatic Facility at Old Dominion University (ODU) in Norfolk, VA, USA, all captured animals were kept in a 114 L circular holding tank (Angle

Livewells, Aquatic Ecosystems, Inc., Apopka, FL, USA) fitted with a battery-powered aerator (Model B-3, Marine Metal Products Co., Inc., Clearwater, FL, USA). At ODU, animals were held in aerated 1700-L recirculating seawater systems with biological and mechanical filtration. Seawater in the transport and holding tanks was maintained at temperatures of 19–22°C and salinities of 29–32‰, similar to values at collection sites. A moderate current flow was present in the holding tanks, and squid were fed live grass shrimp (*Palaem onetes pugio*) and mummichogs (*Fundulus heteroclitos*) (Hanlon 1990). All squid were kept in holding tanks for at least 48 h prior to experimentation, and only animals that appeared healthy and active were selected for this study.

Electrophysiological recordings

We measured pressure inside the mantle cavity and *en passant* extracellular recordings from the stellar nerve during jetting as described previously (Otis and Gilly 1990; Neumeister et al. 2000; Li and Gilly 2019). Squid were anesthetized in 1.8% $MgCl_2$ in aerated seawater for 3 min until minimal response to physical touch was observed. The squid were then placed ventral-side down on a piece of paper towel on the bottom of the surgery dish filled with seawater to prevent the suckers on the squid's arms from attaching to the dish, and a 5 × 5 mm plug of dorsal mantle tissue was surgically removed over the lateral, posterior region of the stellate ganglion. Surgery did not last more than 4 min, and animals fully recovered in aerated seawater within 30 min of surgery. Although some seawater exited through the surgery aperture during jets, it was present throughout all experiments in all animals tested, so our data do not include the effects of this aperture.

After recovery from surgery, squid were again exposed to 1.8% $MgCl_2$ in aerated seawater for 2 min to relax specimens before tethering. Based on established methods, squid were restrained by affixing the midline of the dorsal mantle surface to an acrylic supporting platform with cyanoacrylate cement (Otis and Gilly 1990). The platform was suspended in the experimental tank (50 × 25 × 32 cm), and the squid could still contract its mantle and produce jets normally underneath the platform but remain stationary. Tethering allowed attachment of the instrumentation to record neural activity and pressure inside the mantle cavity.

Pressure recordings were made based on established methods (Otis and Gilly 1990) using a pressure transducer (40PC006G, Honeywell, Morris Plains, NJ, USA) coupled to a syringe needle (20 gauge) filled with mineral oil and inserted through the mid-posterior of the dorsal mantle into the mantle cavity. The voltage output of the pressure transducer was calibrated to known pressure values provided by a pressure injector (Medical Systems Corporation, Harvard Apparatus, Holliston, MA, USA).

Conventional extracellular recordings of nerve activity were made using a polypropylene suction electrode (Ag: AgCl wires) that was inserted through the hole over the ganglion and attached to the second-hindmost stellar nerve within 5 mm of its emergence from the stellate ganglion. Neural signals were sent through an AC-coupled amplifier (DP-301, Warner Instrument Corp., Hamden, CT, USA) that applied low-pass (3 kHz) and high-pass (0.1 Hz) filtering and an amplification of 1000.

Pressure and neural recordings were simultaneously sampled at 10 kHz by a digital-to-analog converter (DAQ) interface (NI USB-6341, National Instruments, Austin, TX, USA) using commercially available software (LabVIEW SignalExpress, National Instruments). Signals were recorded for 12 or 32 s, which included 2 s of recording prior to triggering. Pressure recordings were smoothed using a moving average spanning across 501 points (0.05 s) in MATLAB (version 2014b, The MathWorks Inc., Natick, MA, USA), since this method preserved the shape of the curve most closely. Neural signals were not smoothed for analysis.

Wake visualization

DDPTV (Pereira et al. 2000, 2006; Couch and Krueger 2011) was used to visualize wake structures of jets. The experimental tank was filled with aerated seawater at the same temperature and salinity as that of the holding tanks and seeded with neutrally buoyant 50 μm light-reflective polyamide particles (Dantec Dynamics, Skovlunde, Denmark). A V3V-8000 probe (TSI, Inc., Shoreview, MN, USA; three 12-bit 2048 × 2048-pixel cameras) was positioned in front of the experimental tank to capture a side view of the tethered squid. A Twins Brilliant B 380 mJ/pulse Nd: YAG dual-cavity laser (Quantel Laser, Bozeman, MT, USA) illuminated a 14 × 14 × 10 cm region of the tank at a paired-pulse rate of 5 Hz. The V3V-8000 probe was synchronized with the laser using a 610,035 LaserPulse generator (TSI, Inc.), and paired DDPTV images ($\Delta t = 2$ ms between an image pair) of the squid's jets were captured at 5 Hz.

We used INSIGHT 4G V3V software (TSI, Inc.) to identify 3D particle locations and calculate particle displacements by following established protocols (Pereira et al. 2000; Troolin and Longmire 2010). Overall, 80,000–100,000 particles were identified in each image, and 40,000–55,000 particles among all three cameras were matched to form triplets (50–55% of identified particles). To track particles between each image

pair, we used the relaxation method, an iterative tracking method that searches for the most probable link between particles across two frames, available in INSIGHT 4G V3V software due to its more accurate results at low and high particle displacements and higher robustness and efficiency than nearest neighbor or neural network tracking methods (Pereira et al. 2006). We obtained 11,000–12,000 particle vectors in the final imaging volume (114 × 136 × 96 mm), and a median filter (level 6) and global range filter (–0.8 to 0.8) were applied to remove large, erroneous vectors. The vectors were interpolated onto a structured grid using a Gaussian weighting interpolation available in INSIGHT 4G V3V to provide data on vorticity and vortex location. A voxel size of 16 mm, % overlap of 99%, and a smoothing factor of 1 were used for the Gaussian weighting interpolation in these experiments.

Experimental trials

Each animal experienced multiple experimental trials to document as many jet sequences as possible, and trials ceased when animals no longer reliably produced jets. There was a rest period of at least 2 min between trials. The length of an experimental trial was determined by the amount of time the DAQ interface was set to record pressure and neural signals (12 or 32 s), and paired laser pulses were fired at 5 Hz during that timeframe to illuminate particles and visualize wakes. Because giant axon jets were most consistently observed at the beginning of a laser firing bout, firing ceased in the middle of some trials and recommenced after a resting period of darkness in an attempt to elicit more giant axon jets. Room lights were kept off during experiments, so the laser was the only source of light that could stimulate the animal. No other external stimuli were applied.

Synchronization of measurements

In order to synchronize wake visualization from the V3V probe and recordings of pressure and neural activity, an LED panel was turned on and then off after the V3V probe began capturing image pairs. The illuminated LED panel prompted the DAQ interface to capture 2 s of pressure and neural signals prior to LED illumination and up to 30 s after by affecting a photoresistor in an Arduino-controlled circuit. The time at which the DAQ interface initiated the recording corresponded with the first instance of the illuminated LED panel in V3V image pairs, thus allowing subsequent image pairs at a known sampling frequency to be synchronized with the simultaneous pressure and neural signals.

Analysis

Following established protocols (Bartol et al. 2016), we used in-house MATLAB routines to compute the specific impulse (**I**) associated with fully formed vortical flows generated by squid from DDPTV data. **I** of an isolated vortex was computed from following equation:

$$\mathbf{I}/\rho = \frac{1}{2}\int_V \mathrm{x} \times \omega \, dV, \tag{1}$$

where **x** is the position vector, $\boldsymbol{\omega}$ is the vorticity vector ($\omega = \nabla \times \mathbf{u}$, where **u** is the velocity vector), ρ is the fluid density, and the integral is computed over the volume, V, of the vortex (Saffman 1992). The 3D volume surrounding the vortex of interest was visually determined and selected through a MATLAB graphical user interface. Care was taken to minimize influence of measurement noise around the jet of interest, and the integral was computed over the selected volume. The magnitude of **I** was computed as $\sqrt{I_x^2 + I_y^2 + I_z^2}$, where I_x, I_y, and I_z are components of the impulse vector in the x, y, and z coordinate directions, respectively. In the case of having more than one image frame with fully formed jet wakes, the frame with the maximum impulse was selected to represent that jet in subsequent analyses.

Time-averaged force magnitude was calculated as impulse magnitude divided by the jet cycle period, T_j, defined as the contraction period plus refilling period. Although refilling does not contribute greatly to impulse generation, propulsion from a jet produced by the mantle contraction has to last through the refilling period to be meaningful for a swimming animal. T_j was determined by the number of seconds from trough to trough in the pressure recording indicating a jet cycle corresponding to the timing of a DDPTV image pair. Jet angle, θ, with respect to the x-axis was determined as:

$$\theta = \arctan\left(I_y/I_x\right) \tag{2}$$

using the x- and y-components of impulse. With the aperture of the funnel treated as the origin, a vertically downward jet parallel with the y-axis has an angle of –90° and jet angles of 0° and –180° parallel with the x-axis are completely tail-first or arms-first, respectively. All figures depicting wake visualizations from DDPTV data were created using Tecplot 360 (Tecplot Inc., Bellevue, Washington, USA). All histograms were produced in MATLAB.

A linear mixed-effects model was used to compare jet angle, cycle period, impulse magnitude, and force magnitude for jets initiated by giant axon activity with those initiated by non-giant axon activity. Because residuals of each jet feature were not normally distributed, all data were log transformed prior to analysis with the

Table 1 Occurrences and percentage of total jets based on direction per neural pathway. A jet angle threshold of $\theta \leq -100^\circ$ was used for a jet aimed toward the tail-end of the squid for arms-first swimming, $-100^\circ < \theta < -80^\circ$ for a downwards jet, and $\theta \geq -80^\circ$ for a jet aimed toward the arms for tail-first swimming

Direction	Giant axon system (n = 17 jets)	Non-giant axon system (n = 144 jets)
Arms-first swimming	13 (76.5%)	102 (70.1%)
Downwards jet	0 (0%)	16 (11.1%)
Tail-first swimming	4 (23.5%)	26 (18.1%)

model. Jet angle measurements were multiplied by −1 to produce equivalent positive values for the log transformation. Accounting for repeated measures and unequal sample size between the two neural pathways, the model treated neural type as the predictor, whereas the identity of individual laser-firing events and each bout of laser firing after darkness were random effects. Degrees of freedom were approximated by Satterthwaite's method to minimize Type 1 error (Luke 2017), and P-values (significance threshold of $P < 0.05$) were computed from t-values output from the linear mixed-effects model.

Results

Wake structures in tethered squid

A total of 161 jets from 3 individual squid were considered for this study based on the criteria of neural signals and pressure measurements being of satisfactory quality and wake structures appearing to be fully developed. Of these jets, 144 were associated with only non-giant axon activity and 17 with only giant axon activity. The majority of jets from both neural pathways were directed toward the tail-end for arms-first swimming (Table 1). Representative examples of jets driven by giant axon and non-giant activity are shown in Figs. 2 and 3, respectively. Three of these examples depict arms-first jets (Figs. 2B, C, and 3C), and one shows a downwards jet (Fig. 3B).

Nearly all jets were pulses short in length based on the associated velocity vector fields (Figs. 2Bi, Ci, and 3Bi) and velocity magnitude isosurface depictions (Figs. 2Bii, Cii, and 3Bii). A key signifier of a short pulse was the presence of a single 3D vortex ring shown in the vorticity magnitude isosurface plots (Figs. 2Biii, 2Ciii, and 3Biii).

Some jets exhibited characteristics of possibly being more intermediate in length, with a pulse followed by a small trailing structure (Figs. 3Ci and Cii). In these cases, a leading-edge vortex ring (Fig. 3Ciii, caret) followed by a trailing vortical structure (Fig. 3Ciii, bracket) was present. We did not detect any elongated wake structures that exceeded those of the intermediate length jets. Vortex rings were present in all analyzed wakes, and they sometimes appeared as interconnected ring structures, especially if jets were produced in quick succession (not shown).

Recruitment of giant vs. non-giant axons

The laser was turned on and off multiple times within a trial. Because strobe flashes can induce giant-axon mediate escape jets in another Loliginid squid (Otis and Gilly 1990), jets were also analyzed based on elapsed time after the initiation of laser firing to reveal which jets were associated with giant vs. non-giant neural activity. More than 60% of jets driven by giant axons occurred at the very beginning of laser firing, whereas jets associated only with non-giant axons generally occurred a few seconds into a laser firing bout and became more frequent as time elapsed (Fig. 4).

Comparison of jet characteristics and bulk properties between neural pathways

Jets were characterized by angle (θ) and cycle period (T_j), as described in the methods. Jet angle was not significantly different for jets driven by giant vs. non-giant axons ($P = 0.874$, Fig. 5A, Table 2), nor was jet cycle period ($P = 0.246$, Fig. 5B, Table 2). Bulk properties of the 3D jet wake allowed for calculation of triaxial impulse and force. Computed from the x-, y-, and z-components of the wake's impulse, the difference in impulse magnitude between the two neural pathways was near significant ($P = 0.055$, Fig. 6A, Table 2). Jets associated with the giant axon system had, on average, a greater impulse magnitude than those of the non-giant system. Dividing impulse magnitude by jet cycle period to compute force magnitude, we found no difference between the two neural pathways ($P = 0.157$, Fig. 6B, Table 2).

Discussion

Jets elicited with laser as a stimulus

Giant axon jets were infrequent (10.6% of all analyzed jets) and disproportionately occurred at the onset of laser firing (Table 1 and Fig. 4). Though jets can be elicited by several stimuli, only a strobe flash reliably elicits jets initiated by the giant axon system in lab set-

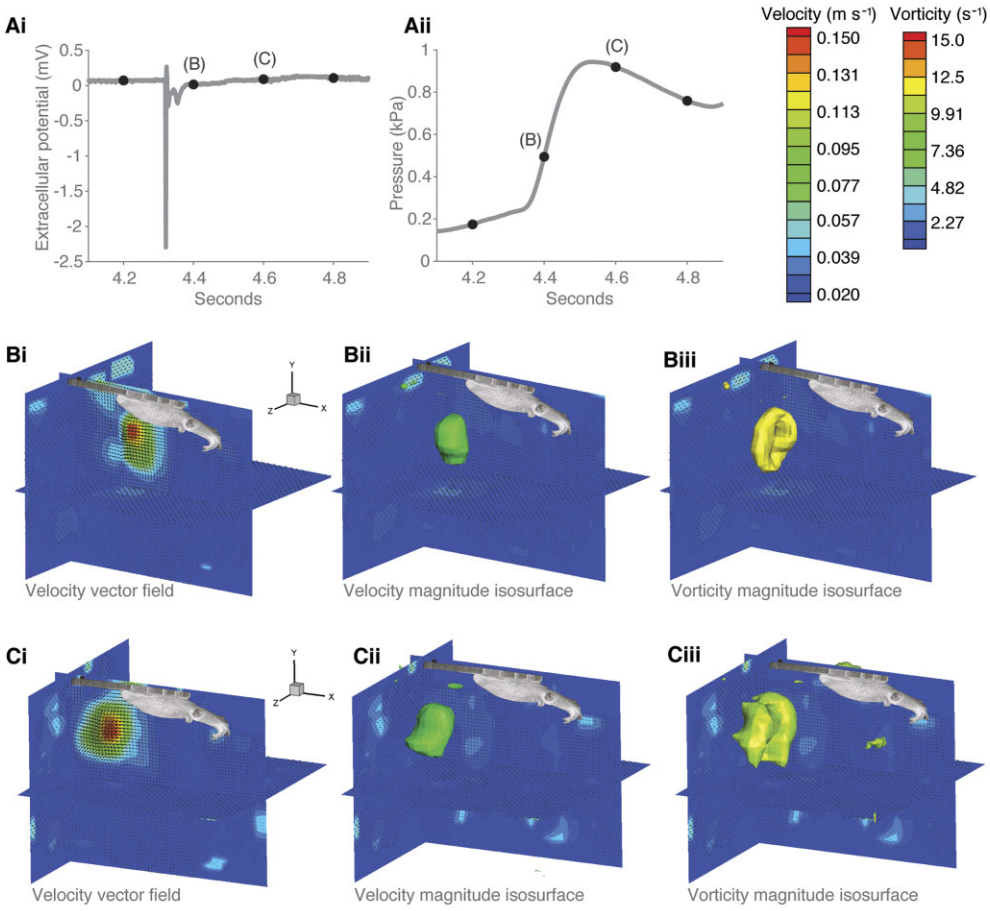

Fig. 2 Representative example of (Ai) neural, (Aii) pressure, and (B, C) DDPTV images of wake structure data from an arms-first jet associated with giant axon activity. (A) Black dots signify times at which frames were captured for wake structure data, with frames at 4.4 and 4.6 s shown in panels B and C, respectively. (Ai) Giant axon activity is characterized by a large spike immediately preceding mantle contraction with minimal subsequent neural activity, and (Aii) the resultant pressure inside the mantle cavity peaks quickly. (Bi, Ci) Velocity contour slices and (Bii, Cii) velocity magnitude isosurfaces depict a jet characterized by a short pulse of water. The vorticity of this jet appears as an isolated vortex ring, as illustrated by Biii and Ciii, showing the vorticity magnitude isosurface. In this example, both frames exhibited fully developed wakes for the same jet, so the frame associated with maximum impulse would be used for subsequent analyses.

tings (Otis and Gilly 1990). Olfactory, electrical, or mechanical stimuli elicit jets initiated by a burst of motor activity in the non-giant system, though giant axon activity can be recruited about 50 ms after the onset of non-giant firing (Otis and Gilly 1990). Here, we found the laser pulses to function similarly to a strobe flash, because the first jet in a bout of repetitive jetting was initiated by the giant system with no obvious non-giant activity. Nearly all subsequent secondary jets arose from the non-giant system acting alone (Fig. 4). Although it is possible to repeatedly elicit jets initiated by the giant axon system in response to a strobe flash, stimuli must be administered at least 1 min apart in order to avoid fatigue or habituation (Li and Gilly 2019). Because the dual-cavity laser fired at 5 Hz for a duration of 10 or 30 s, it is possible that jets being produced in response to such a rapid stimulus would not allow the giant system enough time to recover. The non-giant system, on the other hand, might be able to handle producing jets in quick succession, consistent with its ability to produce graded muscle contractions.

Analysis of the muscle fiber types involved in jetting could also shed light on the proportion and timing of jets from the two neural systems during a bout of laser firing. Different muscle fiber types have been characterized in mantle tissue, namely two types arranged in three distinct layers. The thin inner and outer portions, known as the superficial mitochondria-rich (SMR) layers, comprise about 25% of the mantle's mass and surround a much thicker middle region, called the central mitochondria-poor (CMP) layer (Bone et al. 1995). Compared often to red and white muscle of fish, the SMR layers are aerobic and mainly used in slow, respiratory swimming, whereas the CMP layer is characterized

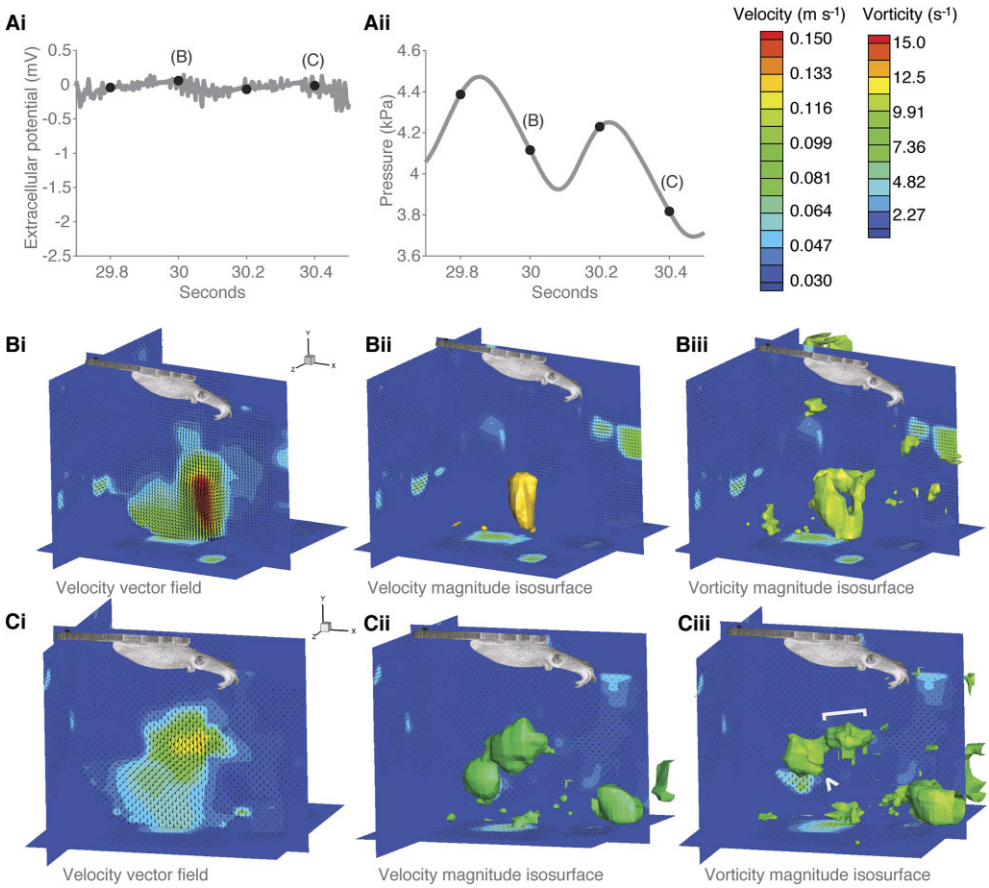

Fig. 3 Representative example of (Ai) neural, (Aii) pressure, and (B, C) DDPTV images of wake structure data from jets associated with non-giant axon activity. (Ai) In contrast to giant-axon activity shown in Fig. 2, non-giant axon activity is characterized by repetitive bursts of small-magnitude spikes, and (Aii) the corresponding pressure inside the mantle cavity shows jets made in quick succession. Frames at 30 and 30.4 s were selected because wakes only appeared to be fully developed during the decreasing pressure phase, and they are depicted in panels B and C, respectively. At 30 s, the jet's (Bi) velocity vector field and (Bii) velocity magnitude isosurface panels show a short downward pulse corresponding to (Biii) a single vortex ring apparent in the vorticity magnitude isosurface panel. In contrast, at 30.4 s, the jet exhibits (Ci, Cii) a possible intermediate-length arms-first pulse and (Ciii) a ring traveling leftward (caret) with a short trailing vortical structure behind it (bracket).

by high glycolytic activity and utilized for stronger mantle contractions and faster jets (Mommsen et al. 1981; Bartol 2001).

CMP fibers are thought to be further divided into two different types based on electrical properties in their excitation (Gilly et al. 1996). One class of muscle fibers, presumed to be from the CMP layer, is rich in sodium channels and generates fast, all-or-none muscle twitches. This fiber type is likely associated with the giant axon system, thus serving as the basis for strong mantle contractions. Another set of fibers devoid of sodium channels appears to be a separate type of CMP fiber showing graded excitability related to repetitive stimulation of non-giant axons. The distribution of giant and non-giant jet occurrences in this study (Fig. 4) could reflect basic differences in the thresholds that regulate excitation of these two CMP fiber types. A severe enough stimulus, such as the laser firing and suddenly disrupting darkness, could exceed the threshold for giant axon excitation and activation of the sodium-rich CMP fibers for short-latency jets. When the stimulus is no longer novel, it may fail to exceed the threshold needed to utilize the giant pathway, or the giant axon pathway may fatigue without sufficient recovery time between stimuli. In either case, jets immediately following the initial giant axon pathway response would be the result of repetitive firing in the non-giant pathway to excite the other class of CMP fibers.

Despite potential fatigue and/or habituation of the giant axon pathway, the laser was able to elicit jets from different motor pathways as expected based on the muscle fiber types present in squid. Future studies could consider reducing the firing frequency of the laser and/or including longer resting periods without laser firing within each trial to allow for sufficient recovery, which would probably increase the chances of

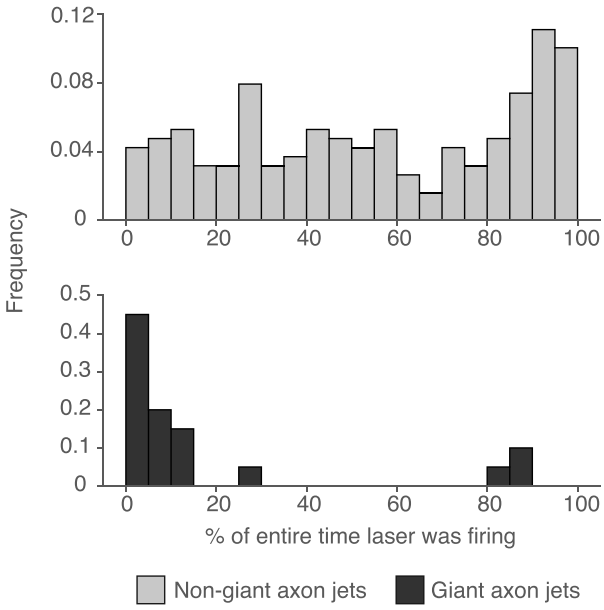

Fig. 4 Jet occurrence by neural type during a bout of laser firing. Giant axon jets ($n = 17$) tended to occur near the start of laser firing, whereas non-giant jets ($n = 144$) were prevalent throughout a laser bout and became more frequent as time elapsed. The total time the laser was firing ranged from a minimum of 6.4 s to a maximum of 30 s.

documenting giant axon jets. Another idea would be to employ a near-infrared laser, to which the squid might be visually insensitive, allowing the use of other visual, olfactory, and electrical stimuli to elicit a wider variety of jets, including those arising from combined input of both neural pathways.

Wake structures compared between tethered and free-swimming squid

Previous work visualizing jet hydrodynamics in squid has identified a variety of wake structures in free-swimming squid (Anderson and Grosenbaugh 2005; Bartol et al. 2009b, 2016). Studies utilizing DDPTV to reveal 3D wake structures of *L. brevis* provide the most direct comparison with our dataset based on tethered animals. All wakes observed from tethered animals possessed 3D vortex ring structures, typically as a single ring but sometimes as interconnected ring structures, especially if jets were produced in quick succession. Similar vortex rings were observed in free-swimming squid of the same species (Bartol et al. 2016), and the size range of our tethered animals (5.9–7.0 cm DML) was well within that of the free-swimming animals (3.5–10 cm DML).

Although wake structures in tethered squid are similar to a subset of those in free-swimming animals of the same species, some differences merit consideration. In addition to small singular pulses with a single vortex ring (Figs. 2Biii, Ciii, and 3Biii), tethered animals sometimes produced structures of intermediate length, with a vortex ring trailed by a short vortical structure (Fig. 3Ciii). However, jets were never long enough to match the elongated jet structures with a vortex ring pinching off from a trailing jet as seen in free-swimming squid (Bartol et al. 2009b, 2016). Three factors are probably relevant. First, some water could have escaped through the small hole on the dorsal surface of the mantle for neural recordings, thus reducing the flow through the funnel during jets. Second, animals in this study were often producing jets near maximum frequency (1–2 Hz), and it is possible that there was not enough time for animals to fully refill their mantle cavities to produce a jet of larger volume to draw out an elongated jet wake. Third, the majority of jets observed from tethered animals occurred when the funnel was aimed toward the tail-end for arms-first swimming. Elongated jets in free-swimming animals are typically observed when the squid is oriented tail-first, with arms-first jetting primarily involving short vortex ring pulses, even at high swimming speeds (Bartol et al. 2016). Indeed, a 3D velocimetry dataset collected during a preliminary phase of the project when a squid swam predominantly in the tail-first mode included a number of longer jets with leading edge ring structures (Supplemental Fig. 1). These data were not considered in our analyses because excessive equipment noise in these early trials affected neural signals. Therefore, the low percentage of tail-first jets from tethered squid likely was a major reason for the absence of elongated wake structures.

Neural pathways can influence a jet beyond kinematics

Our hydrodynamic data extend upon previous work, which has established a direct role of the giant and non-giant axon systems on the kinematics of a jet through modulation of muscle twitch and pressure inside the mantle cavity driving a mantle contraction. Innervation from the giant axon system, characterized by its all-or-none nature, elicits large muscle twitches (Gilly et al. 1996) and mantle pressure (Otis and Gilly 1990) and underlies powerful escape jets (Packard 1969). The non-giant system must show repetitive activity to generate significant muscular response, and summation produces a graded range of mantle contractions to levels equal to (or exceeding) those of the giant axon system (Otis and Gilly 1990; Gilly et al. 1996). We saw a similar division of neural influence on certain jet properties in this study, specifically impulse magnitude and time-averaged force magnitude.

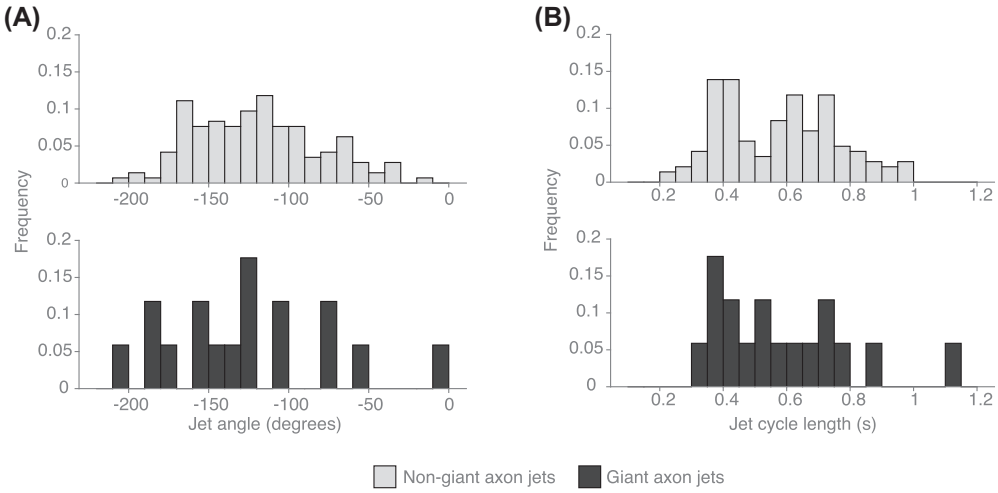

Fig. 5 Frequency distributions of jet characteristics between the two neural pathways (giant, $n = 17$; non-giant, $n = 144$). Neither (A) jet angle, θ, nor (B) jet cycle period, T_j, were significantly different between giant and non-giant axon jets.

Table 2 Mean ± standard deviation of jet features measured from all jets across three individuals. An asterisk indicates $P \leq 0.055$ between jets of the two neural systems based on the linear mixed-effects model

Feature	Giant axon system ($n = 17$ jets)	Non-giant axon system ($n = 144$ jets)
Jet angle (degrees)	−125.7 ± 51.9	−119.9 ± 39.4
Jet cycle period (s)	0.58 ± 0.21	0.57 ± 0.18
Impulse magnitude (mN s)*	4.03 ± 1.77	3.27 ± 2.44
Force magnitude (mN)	8.10 ± 5.00	7.21 ± 6.90

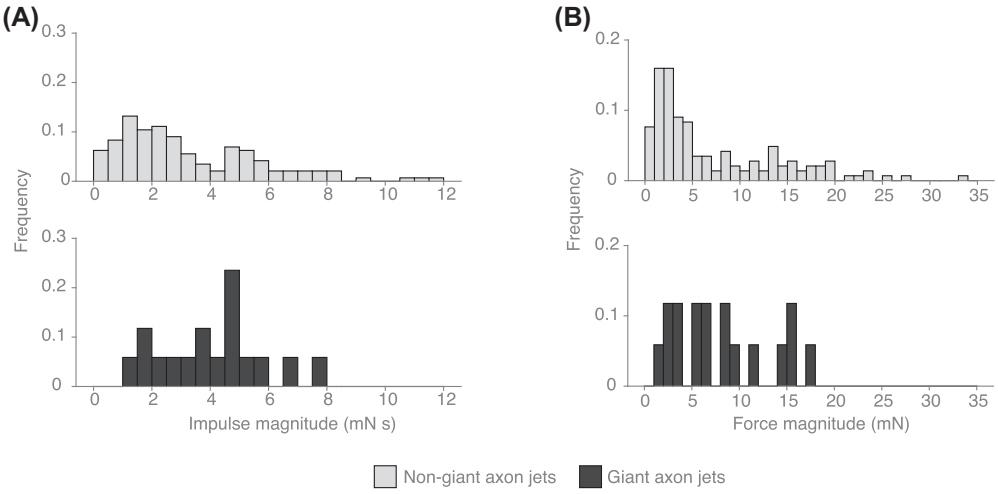

Fig. 6 Frequency distributions of measurements calculated from bulk properties of the jet wake. Giant axon jets ($n = 17$) had on average greater (A) impulse magnitude ($P = 0.055$) than non-giant axon jets ($n = 144$), but (B) force magnitude was not significantly different between the two neural pathways.

Computed from its triaxial components measured from the DDPTV data, impulse magnitude exhibited a near-significant difference between the two neural pathways, with greater impulse for giant axon jets (Table 2 and Fig. 6A). However, the distributions shown in Fig. 6A provide additional insights not captured in the mean values listed in Table 2. Reflecting the all-or-none nature of mantle contractions that arise from giant axon activation, the distribution of impulse magnitude values was tighter, with smaller standard deviation and range for giant axon jets (Table 2 and Fig. 6A). In contrast, impulse magnitude of jets arising from the non-giant

system were on average smaller but more broadly distributed (Table 2 and Fig. 6A). Like the mantle contractions, impulse magnitude associated with non-giant jets could exceed maximum values from giant axon jets (>8 mN s in Fig. 6A), a feature shared in pressure measurements (Otis and Gilly 1990). These findings suggest that neural pathways and muscular responses can influence hydrodynamic characteristics of the jet downstream of the mantle contraction.

Time-averaged force magnitude, calculated by dividing the impulse magnitude by the jet cycle period, was not significantly different for the two neural pathways. It is possible that jet cycle period measurements introduced more variability, evident by the larger relative standard deviation associated with force magnitude (Table 2). Yet, standard deviation and range of force magnitude were larger for non-giant jets, similar to the situation with impulse magnitude (Table 2 and Fig. 6B).

Thus, these dual motor pathways appear to give rise to a diversity of hydrodynamic output and afford the squid flexibility in its locomotor repertoire: the non-giant axon system can produce a wide range of impulse magnitude, with the giant axon system augmenting output by working in concert with the non-giant system (Otis and Gilly 1990). A large portion of giant axon spikes in our study occurred at the beginning of a jet cycle with no obvious non-giant activity (Figs. 2Ai and Aii). Nonetheless, the greater impulse magnitude associated with the giant system alone suggests that giant axon activity recruited after a jet has been initiated by the non-giant system could enhance impulse under more natural conditions. Because the giant axon system is thought to be under stringent control (Otis and Gilly 1990; Preuss and Gilly 2000), it could be employed under circumstances when this boosting effect would be most needed, such as escaping a threat or lunging arms-first for prey capture.

Implications for jet and fin coordination

Although the non-giant axon system produces lower average impulse than the giant system (Fig. 6A and Table 2), the graded nature of its output could be advantageous when combined with contributions from the fins, which were not considered in our measurements. The fins play a large role in force production, particularly at low swimming speeds (Bartol et al. 2016) and during arms-first swimming (Bartol et al. 2018). They also help with turning (Bartol et al. 2022; Bartol et al. 2023). At low swimming speeds, the giant axon fatigues relatively quickly compared to the non-giant system (Otis and Gilly 1990) and would likely not be the dominant pathway used for slow swimming or fine maneuvers. The non-giant system, on the other hand, could work in coordination with the fins to further tune impulse and force output without recruiting the giant system. For high swimming speeds, especially with tail-first swimming, the fins would play a much smaller role as the squid relies on the jet for the majority of its impulse and force production (Bartol et al. 2016).

Recruitment of fin activity is not directly determined by the giant and non-giant systems and depends instead on motoneurons in a different region of the brain (fin lobes) that project axons through the fin nerves. Little is known about the neuromuscular coordination of mantle and fin activity, but it is clear that the fins decrease flapping frequency and/or wrap around the mantle during high-speed swimming (O'Dor 1988; Hoar et al. 1994; Bartol et al. 2001, 2016, 2018; Stewart et al. 2010) and during giant-axon-driven escape responses (D.H.L. and W.F.G., personal observations). Future research efforts exploring coordination of fin and mantle responses in relation to recruitment patterns in the giant vs. non-giant axon systems would offer insights.

Acknowledgments

We thank Alissa Ganley and Amanda Tumminelli for assistance with animal capture, tank maintenance, and data collection; Sean Fate and the staff at VIMS ESL for field assistance; Paul Krueger for software, technical assistance, and use of his laser; Ben Burford and Robin Elahi for help with statistical analyses; Cydney Tuchton for assistance with preliminary data analysis; and two anonymous reviewers whose comments strengthened the manuscript.

Funding

This project was supported by grants from the U.S. National Science Foundation (ISO-1557754 and IOS-142093 EAGER to W.F.G.; IOS-1557669 to I.K.B.), funds from Stanford University (Friends of Hopkins: Davis Fund, Eugene C. and Aileen E. Haderlie Memorial Award to D.H.L.), and grants from the Conchologists of America and Dr. Earl H. Myers & Ethel M. Myers Oceanographic & Marine Biology Trust to D.H.L.

Supplementary data

Supplementary data available at *ICB* online.

Conflict of interest

All authors declare they have no conflicts of interest.

Data availability

Data are available upon request.

References

Anderson EJ, DeMont ME. 2000. The mechanics of locomotion in the squid Loligo pealei: locomotory function and unsteady hydrodynamics of the jet and intramantle pressure. J Exp Biol 203:2851–63.

Anderson EJ, Grosenbaugh MA. 2005. Jet flow in steadily swimming adult squid. J Exp Biol 208:1125–46.

Bartol IK, Ganley AM, Tumminelli AN, Bartol SM, Thompson JT, Krueger PS. 2023. Turning performance and wake dynamics of neritic squids. Mar Biol 170:73.

Bartol IK, Ganley AM, Tumminelli AN, Krueger PS, Thompson JT. 2022. Vectored jets power arms-first and tail-first turns differently in brief squid with assistance from fins and keeled arms. J Exp Biol 225:jeb244151.

Bartol IK, Krueger PS, Jastrebsky RA, Williams S, Thompson JT. 2016. Volumetric flow imaging reveals the importance of vortex ring formation in squid swimming tail-first and arms-first. J Exp Biol 219:392–403.

Bartol IK, Krueger PS, Stewart WJ, Thompson JT. 2009. Hydrodynamics of pulsed jetting in juvenile and adult brief squid *Lolliguncula brevis*: evidence of multiple jet "modes" and their implications for propulsive efficiency. J Exp Biol 212: 1889–903.

Bartol IK, Krueger PS, Stewart WJ, Thompson JT. 2009. Pulsed jet dynamics of squid hatchlings at intermediate Reynolds numbers. J Exp Biol 212:1506–18.

Bartol IK, Krueger PS, Thompson JT, Stewart WJ. 2008. Swimming dynamics and propulsive efficiency of squids throughout ontogeny. Integr Comp Biol 48:720–33.

Bartol IK, Krueger PS, York CA, Thompson JT. 2018. New approaches for assessing squid fin motions: coupling proper orthogonal decomposition with volumetric particle tracking velocimetry. J Exp Biol 221:jeb176750.

Bartol IK, Patterson MR, Mann R. 2001. Swimming mechanics and behavior of the shallow-water brief squid *Lolliguncula brevis*. J Exp Biol 204:3655–82.

Bartol IK. 2001. Role of aerobic and anaerobic circular mantle muscle fibers in swimming squid: electromyography. Biol Bull 200:59–66.

Bone Q, Brown ER, Usher M. 1995. The structure and physiology of cephalopod muscle fibres. In: Abbott NJ, Williamson R, Maddock L, editors. Cephalopod neurobiology: neuroscience studies in squid, octopus, and cuttlefish. New York, NY: Oxford University Press. p. 301–29.

Couch LD, Krueger PS. 2011. Experimental investigation of vortex rings impinging on inclined surfaces. Exp Fluids 51:1123–38.

Gilly WF, Preuss T, McFarlane MB. 1996. All-or-none contraction and sodium channels in a subset of circular muscle fibers of squid mantle. Biol Bull 191:337–40.

Hanlon RT. 1990. Maintenance, rearing, and culture of teuthoid and sepioid squids. In: Gilbert DL, Adelman Jr. WJ, Arnold JM, editors. Squid as experimental animals. Boston, MA: Springer. p. 35–62.

Hoar JA, Sim E, Webber DM, O'Dor RK. 1994. The role of fins in the competition between squid and fish. In: Maddock L, Bone Q, Rayner JMV, editors.Mechanics and physiology of animal swimming. Cambridge: Cambridge University Press. p.27–44.

Hoover AP, Griffith BE, Miller LA. 2017. Quantifying performance in the medusan mechanospace with an actively swimming three-dimensional jellyfish model. J Fluid Mech 813:1112–55.

Hoover AP, Xu NW, Gemmell BJ, Colin SP, Costello JH, Dabiri JO, Miller LA. 2021. Neuromechanical wave resonance in jellyfish swimming. Proc Natl Acad Sci USA 118:e2020025118.

Krueger PS, Gharib M. 2003. The significance of vortex ring formation to the impulse and thrust of a starting jet. Phys Fluids 15:1271–81.

Krueger PS, Gharib M. 2005. Thrust augmentation and vortex ring evolution in a fully-pulsed jet. AIAA J 43:792–801.

Li DH, Gilly WF. 2019. Hypoxia tolerance of giant axon-mediated escape jetting in California market squid (*Doryteuthis opalescens*). J Exp Biol 222:jeb198812.

Liao JC, Beal DN, Lauder GV, Triantafyllou MS. 2003. Fish exploiting vortices decrease muscle activity. Science 302:1566–9.

Luke SG. 2017. Evaluating significance in linear mixed-effects models in R. Behav Res 49:1494–502.

Mommsen TP, Ballantyne J, Macdonald D, Gosline J, Hochachka PW. 1981. Analogues of red and white muscle in squid mantle. Proc Natl Acad Sci USA 78:3274–8.

Neumeister H, Ripley B, Preuss T, Gilly WF. 2000. Effects of temperature on escape jetting in the squid Loligo opalescens. J Exp Biol 203:547–57.

O'Dor RK. 1988. The forces acting on swimming squid. J Exp Biol 137:421–42.

Otis TS, Gilly WF. 1990. Jet-propelled escape in the squid Loligo opalescens: concerted control by giant and non-giant motor axon pathways. Proc Natl Acad Sci USA 87:2911–5.

Packard A. 1969. Jet propulsion and the giant fibre response of Loligo. Nature 221:875–7.

Pereira F, Gharib M, Dabiri D, Modarress D. 2000. Defocusing digital particle image velocimetry: a 3-component 3-dimensional DPIV measurement technique. Application to bubbly flows. Exp Fluids 29:S078–84.

Pereira F, Stüer H, Graft EC, Gharib M. 2006. Two-frame 3D particle tracking. Meas Sci Technol 17:1680–92.

Preuss T, Gilly WF. 2000. Role of prey-capture experience in the development of the escape response in the squid Loligo opalescens: a physiological correlate in an identified neuron. J Exp Biol 203:559–65.

Saffman PG. 1992. Vortex dynamics. Cambridge:Cambridge University Press.

Stewart WJ, Bartol IK, Krueger PS. 2010. Hydrodynamic fin function of brief squid, Lolliguncula brevis. J Exp Biol 213:2009–24.

Troolin DR, Longmire EK. 2010. Volumetric velocity measurements of vortex rings from inclined exits. Exp Fluids 48:409–20.

Young JZ. 1938. The functioning of the giant nerve fibres of the squid. J Exp Biol 15:170–85.